

1 **Monitoring contractility in single cardiomyocytes and whole hearts with bio-**
2 **integrated microlasers**

3

4 Marcel Schubert^{1,*}, Lewis Woolfson¹, Isla RM Barnard¹, Andrew Morton¹, Becky Casement¹,
5 Gavin B Robertson², Gareth B Miles³, Samantha J Pitt², Carl S Tucker⁴, Malte C Gather^{1,*}

6

7 ¹ SUPA, School of Physics and Astronomy, University of St Andrews

8 ² School of Medicine, University of St Andrews

9 ³ School of Psychology & Neuroscience, University of St Andrews

10 ⁴ The Queen's Medical Research Institute, University of Edinburgh

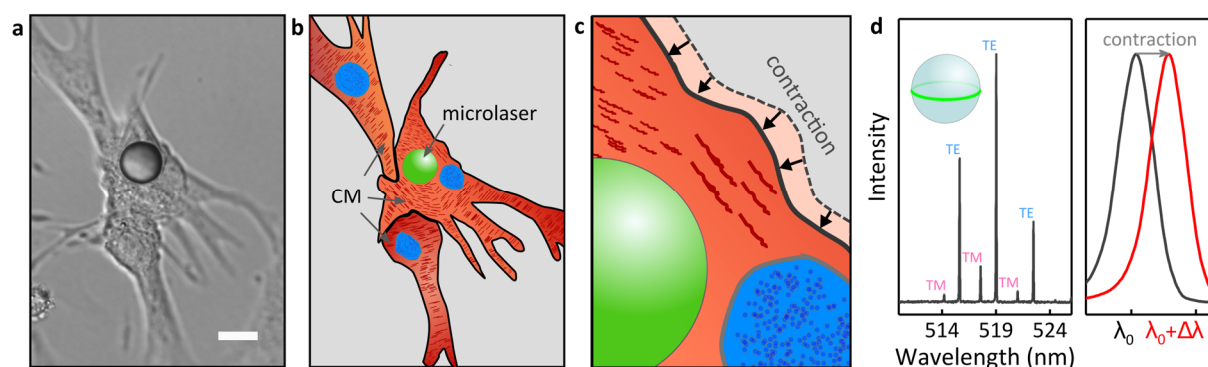
11 * ms293@st-andrews.ac.uk; mcg6@st-andrews.ac.uk

12 **Abstract**

13 **Cardiac regeneration and stem cell therapies depend critically on the ability to locally resolve the**
14 **contractile properties of heart tissue^{1,2}. Current regeneration approaches explore the growth of**
15 **cardiac tissue *in vitro* and the injection of stem cell-derived cardiomyocytes³⁻⁶ (CMs) but scientists**
16 **struggle with low engraftment rates and marginal mechanical improvements, leaving the estimated**
17 **26 million patients suffering from heart failure worldwide without effective therapy⁷⁻⁹. One**
18 **impediment to further progress is the limited ability to functionally monitor injected cells as**
19 **currently available techniques and probes lack speed and sensitivity as well as single cell specificity.**
20 **Here, we introduce microscopic whispering gallery mode (WGM) lasers into beating cardiomyocytes**
21 **to realize all-optical recording of transient cardiac contraction profiles with cellular resolution. The**
22 **brilliant emission and high spectral sensitivity of microlasers to local changes in refractive index**
23 **enable long-term tracking of individual cardiac cells, monitoring of drug administration, and**
24 **accurate measurements of organ scale contractility in live zebrafish. Our study reveals changes in**
25 **sarcomeric protein density as underlying factor to cardiac contraction which is of fundamental**
26 **importance for understanding the mechano-biology of cardiac muscle activation. The ability to non-**
27 **invasively assess functional properties of transplanted cells and engineered cardiac tissue will**
28 **stimulate the development of novel translational approaches and the *in vivo* monitoring of**
29 **physiological parameters more broadly. Likewise, the use of implanted microlasers as cardiac**
30 **sensors is poised to inspire the adaptation of the most advanced optical tools known to the**
31 **microresonator community, like quantum-enhanced single-molecule biosensing or frequency comb**
32 **spectroscopy¹⁰.**

33

34 To elucidate CM contractility under various experimental conditions, we explored the integration of
35 WGM microlasers as multifunctional optical sensors. Chip-based fibre- and prism-coupled WGM
36 biosensors have previously achieved sensitivities down to the single molecule and protein level^{11,12}.
37 However, their potential for intracellular sensing remains largely unexplored as integration into
38 biological systems requires further miniaturization, self-sustained and prolonged emission of light, and
39 data analysis protocols with improved robustness. Recently, microlasers were proposed as novel
40 optical tags to uniquely discriminate hundreds of thousands of cells^{13–16}.

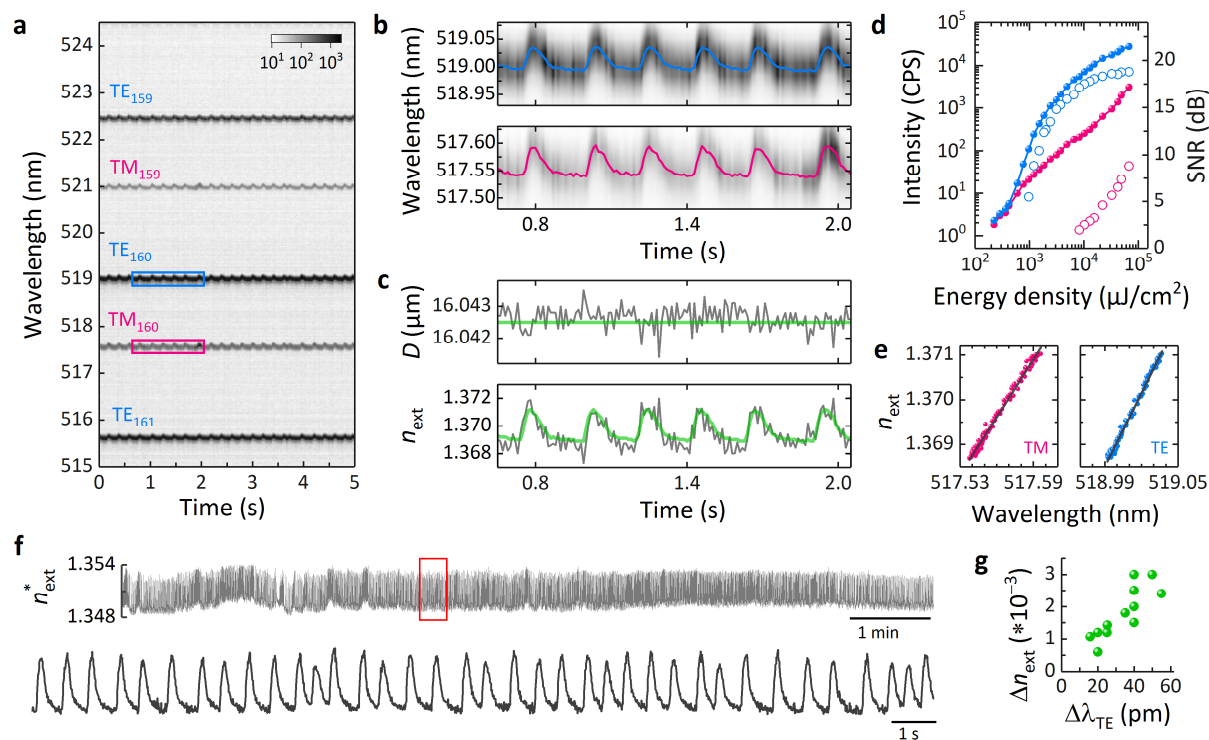


41

42 **Fig. 1 | Principle of microlaser-based intracellular sensing in neonatal mouse CMs.** **a**, DIC microscopy and **b**,
43 schematic illustration of a group of neonatal CMs and an intracellular microlaser (green sphere). **c**, Magnified
44 view visualizing the contractile movement of the cell around the microlaser, due to the action of sarcomeres
45 (dark red fibres). **d**, WGM spectrum of a microlaser showing multi-mode lasing in pairs of TE- and TM-modes
46 (left). WGMs are localized within an equatorial plane close to the surface of the microlaser (inset, green line).
47 Zoom-in onto one peak in the WGM spectrum illustrating the red-shift in lasing wavelength upon CM contraction
48 (right; $\lambda_0 = 519$ nm, $\Delta\lambda = 50$ pm). Scale bar, 15 μ m.

49 Fig. 1 illustrates the general principle of our laser-based contraction sensor. Brightly fluorescent
50 polystyrene microspheres with a diameter between 10 to 20 μ m were used as efficient and robust
51 microscopic WGM lasers that show multi-mode emission under remote optical pumping.¹³ These
52 lasers were actively internalized by different types of cardiac cells (Supplementary Figs. 1 and 2). Upon
53 CM contraction, individual peaks in the emission spectrum of the lasers showed a spectral red-shift
54 (typically, $\Delta\lambda \approx 50$ pm; Fig. 1d). Due to the bright and narrowband laser emission, the wavelength of
55 each lasing mode can be monitored rapidly (acquisition rate, 100 Hz) and accurately (spectral
56 resolution, 1 pm), revealing pulse-shaped perturbations in lasing wavelength synchronized across all
57 modes and coincident with the spontaneous contractions of the cell (Figs. 2a, 2b and Supplementary
58 Video 1). By tracking at least 2 pairs of TE and TM lasing modes and fitting their position to an optical
59 model, we independently determined the diameter D of each microsphere and the average external
60 refractive index n_{ext} , i.e. the refractive index (RI) of the volume probed by the evanescent component
61 of the WGM (Fig. 2c and Supplementary information). This revealed a characteristic increase in RI
62 during cell contractions. Statistical analysis of the microsphere diameter was then applied to reduce

63 the effect of fitting noise before reiterating the RI calculation. This significantly improved the signal
 64 quality and thus allowed the detection of minute changes in n_{ext} , with a RI resolution of 5×10^{-5} ,
 65 which rivals the most sensitive cell refractometric techniques currently available¹⁷.



66

67 **Fig. 2 | Transient red-shifts of microlaser emission are caused by changes in intracellular refractive index.** **a**,
 68 Contour plot of the temporal evolution of the lasing spectra for an intracellular microlaser, measured with 10 ms
 69 temporal resolution. **b**, Magnified view of the areas highlighted in **a**, for a pair of TM (pink) and TE (blue) WGMs.
 70 The coloured lines show the centre position of each mode obtained from peak fitting. Shifts to longer
 71 wavelengths coincide with spontaneous CM contractions. **c**, Calculated diameter (top) of the microlaser (grey)
 72 and time-averaged diameter (green). External refractive index n_{ext} (bottom) calculated with unrestricted
 73 microlaser size (grey) and by applying the fixed mean diameter of the microlaser (green). **d**, Typical threshold
 74 characteristics (left axis, closed symbols) for the brightest TE mode (blue) and the least intense TM mode (pink)
 75 of 4 tracked lasing modes. Lasing thresholds are about $500 \mu\text{J}/\text{cm}^2$ (TE) and $20 \text{ mJ}/\text{cm}^2$ (TM), respectively. Signal-
 76 to-noise ratio (SNR) (right axis, open symbols) of the same modes under single pulse excitation. **e**, Mode
 77 calibration of the 2 modes shown in **b** using data from 6 contractions. From the slope of the linear fit (grey line),
 78 a sensitivity S of 0.0429 nm^{-1} and 0.0549 nm^{-1} is obtained for the TM and TE mode, respectively. **f**, Continuous
 79 single cell monitoring over 10 min (top) at $2 \text{ mJ}/\text{cm}^2$ (corresponding to 2 nJ/pulse) and magnified view of the
 80 20 s window indicated by the red rectangle (bottom). **g**, Average refractive index change (Δn_{ext}) between
 81 resting phase (diastole) and peak contraction (systole) for $n=12$ cells plotted over the corresponding average
 82 change of the dominant TE WGM ($\Delta\lambda_{\text{TE}}$).

83

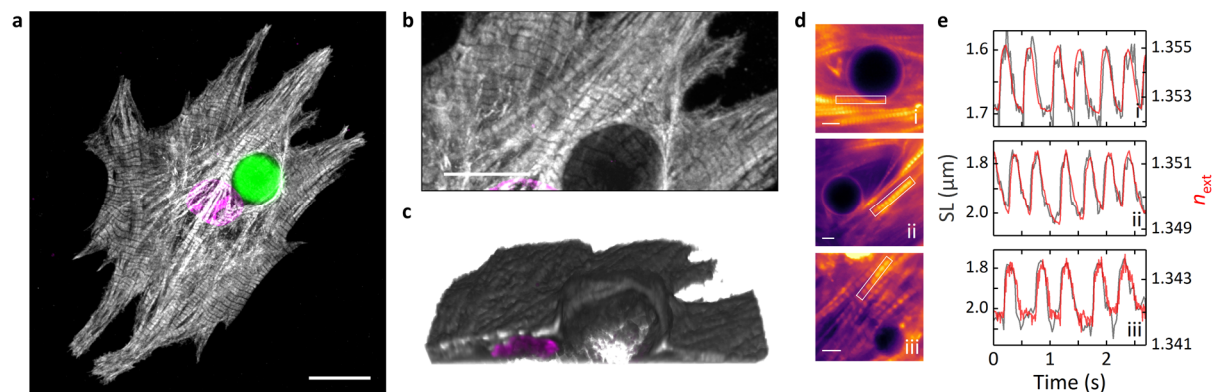
84 Of the 2 pairs of TE and TM lasing modes required for fitting to the optical model, the brightest mode
 85 typically has a lasing threshold below $1 \text{ mJ}/\text{cm}^2$ (corresponding to $<1 \text{ nJ}/\text{pulse}$, Fig. 2d). Above
 86 threshold, this mode rapidly increased in intensity to become 2 to 3 orders of magnitude more intense
 87 than the bulk fluorescence of the microlaser. Single pulse excitation at around $1 \text{ mJ}/\text{cm}^2$ can be

88 therefore used to accurately determine the spectral position of this mode (Supplementary Fig. 3). By
89 comparison, the least intense mode of the 2 pairs required 10 to 50 times higher pump energy to pass
90 the lasing threshold and to determine its spectral position with sufficient accuracy to ensure
91 convergence of our fitting algorithm. Furthermore, we found that the periodic changes in RI due to
92 cardiomyocyte contraction can be utilized to determine the sensitivity (S) of each laser mode (Fig. 2e,
93 Supplementary Fig. 4). Using S and tracking the spectral position of just the brightest lasing mode then
94 allows calculation of a linearly approximated external refractive index n_{ext}^* , which means the pump
95 energy can be reduced by at least one order of magnitude. This calibration protocol enabled real time
96 RI sensing, allowed continuous yet non-disruptive read-out (Fig. 2f) and greatly improved the
97 robustness of the approach under challenging experimental conditions (see below).

98 Analysis of multiple CMs furthermore revealed that contractions consistently led to an increase of
99 cellular RI which indicates the presence of a highly reproducible physiological process that alters the
100 optical properties of CMs depending on the activation state of their contractile elements (Fig. 2g).

101 To identify the origin of the RI increase during CM contraction we analysed the 3D organization of
102 myofibrils, cellular organelles which comprise repeating contractile elements called sarcomeres. It is
103 generally assumed that CMs contract under isovolumetric conditions¹⁸, yet X-ray diffraction
104 experiments have revealed a linear relationship between sarcomere length and volume of the
105 myofibril unit cell indicating that cell contractions significantly increase the protein density of the
106 myofibrils¹⁹. 3D reconstructions of cells showed that microlasers are surrounded by and in direct
107 contact with a dense network of myofibrils (Figs. 3a and 3b, Supplementary Fig. 5), indicating a strong
108 overlap of the contractile protein machinery with the evanescent field of the laser mode, which
109 typically extends up to 200 nm above the resonator surface. Cellular contractility in neonatal CMs was
110 then measured by staining sarcomeric actin filaments and tracking their length change during the
111 contraction cycle, while simultaneously recording spectral shifts in microlaser emission (Figs. 3c and
112 3d, and Supplementary Video 2). We find that the sarcomere length (SL) of myofibrils was directly
113 correlated with n_{ext} , indicating that structural changes inside myofibrils cause the red-shifts in lasing
114 wavelength (Fig. 3b). Given that during contraction n_{ext} increased by up to 0.003 and using the known
115 protein refractive index increment (dn/dc), we further estimated that the observed contraction-
116 induced changes in sarcomere length by about 10% led to a maximum increase in protein
117 concentration of about 8% (Supplementary information). This finding is consistent with the previously
118 reported decrease in unit cell volume¹⁹. It does not contradict observations that the contraction of the
119 whole heart is isovolumetric; during contraction, cardiac cells are likely to expel water from the
120 myofibrils into different parts of the cell or to the extracellular space²⁰, causing a local increase in
121 myofibril density while still conserving the overall tissue volume. The effects associated with

122 sarcomeric lattice spacing and unit cell changes are of great importance for the function of cardiac
123 cells and are believed to play an important role in regulating the length-dependent activation of the
124 heart (Frank-Starling law). Since transient RI profiles provide a direct measure of CM contractility and
125 myofibril density, they provide new insights to the mechano-biology of cardiac cells.

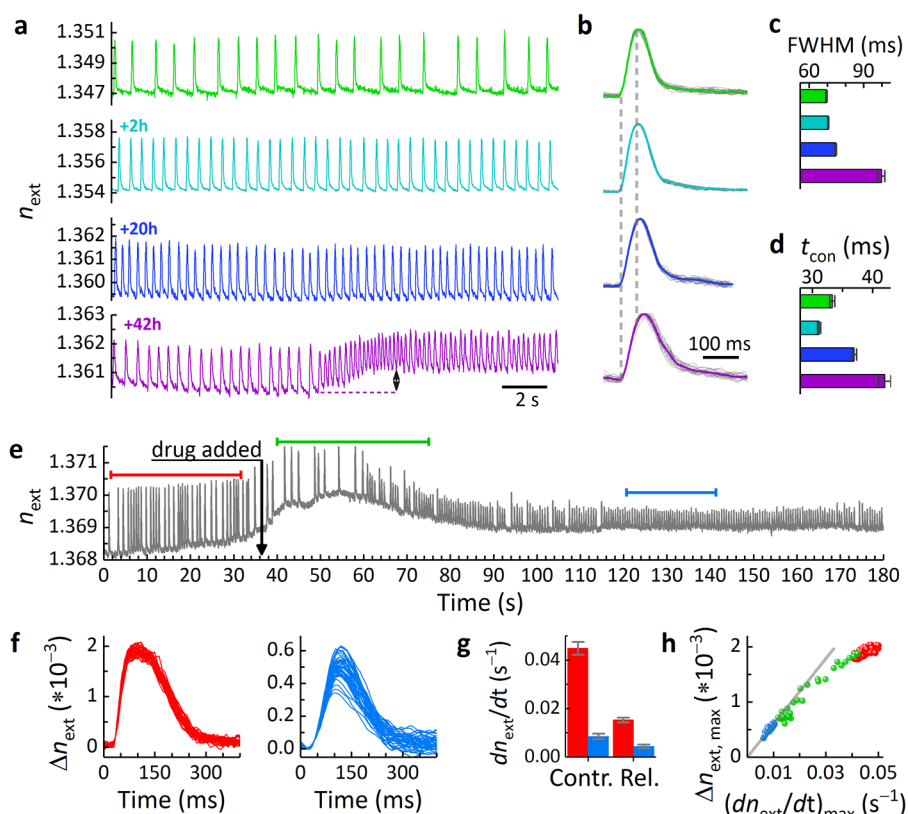


126

127 **Fig. 3 | Microlasers monitor cellular contractility.** 3D arrangement of myofibrils around microlasers in neonatal
128 cardiomyocytes. **a**, Maximum intensity projection showing the sarcomeric protein cTnT (grey), cell nucleus
129 (magenta) and microlaser (green). Scale bar, 15 μm. **b**, Magnified region around the microlaser and **c**, 3D
130 reconstruction of the same area. The microlaser is omitted to show the arrangement of myofibrils more clearly.
131 Scale bar, 10 μm. **d**, Video rate fluorescence microscopy (Supplementary Video 2) of neonatal mouse CMs with
132 labelled myofibrils. Intracellular microlasers are visible as dark circular objects. Scale bars, 5 μm. **e**,
133 Simultaneously acquired temporal profiles of sarcomere length (SL, grey, left axis, extracted from fluorescence
134 profiles of the myofibrils highlighted by the white rectangles in **d**) and n_{ext} (red, right axis, extracted from
135 microlaser spectra). Subfigures labelled according to the images in **d**.

136

137 As the microlaser size provides a unique label to identify and track individual cells over time
138 (Supplementary Fig. 6)¹³, we were able to perform repeated monitoring of single neonatal CMs
139 (Fig. 4a). Normalized contractility profiles (Fig. 4b) showed high temporal regularity with minimal
140 beat-to-beat variations in pulse width (FWHM, Fig. 4c) and contraction time (t_{con} , Fig. 4d). For the
141 example in Fig. 4a, after 42 h, we observe the spontaneous transition into tachycardia which is
142 typically accompanied by increased myocardial tension at elevated beating rates (Bowditch effect), a
143 fundamental process underlying the force-frequency relationship of the heart²¹. At the cellular level,
144 this is caused by increased contractility, which we detected as a step-like increase in the maximum
145 and baseline n_{ext} (black arrow in Fig. 4a), allowing simple quantification of relative protein density
146 changes during the entire contraction cycle.



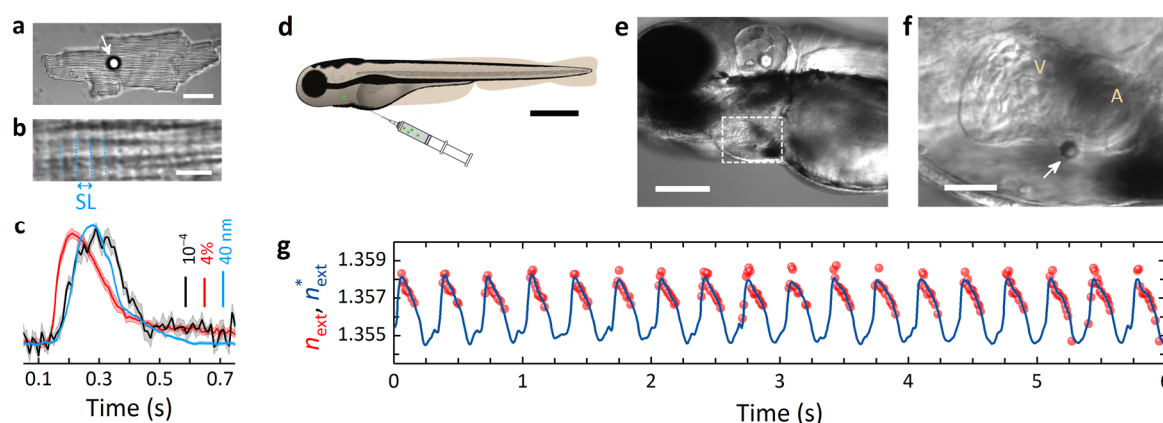
147

148 **Fig. 4 | Single cell tracking and contractility sensing under compromised conditions.** **a-d**, Microlaser-based
 149 tracking and monitoring of a single neonatal CM. **a**, Intracellular n_{ext} trace (green) of an individual CM at start
 150 of experiment, and characterized again after 2 h (cyan), 20 h (blue) and 42 h (violet). The black arrow marks
 151 increased contractility during spontaneous tachycardia. **b**, Normalized n_{ext} profiles of traces shown in **a** for
 152 $n=30-40$ cell contractions (grey lines), overlaid by the averaged n_{ext} profiles (coloured lines). **c**, Full-width-half-
 153 maximum (FWHM) and **d**, average mean contraction time (t_{con}) of the beating profiles in **b**. **e-h**, Effect of
 154 nifedipine on single cell contractility. **e**, n_{ext} trace of a spontaneously beating neonatal CM during administration
 155 of 500 nM nifedipine (black arrow). **f**, Absolute change in refractive index (Δn_{ext}) recorded before (left, red bar
 156 in **e**) and after (right, blue bar in **e**) administration of nifedipine. **g**, Average maximum speed of contraction and
 157 relaxation for the beating profiles shown in **f**. **h**, Peak refractive index change $\Delta n_{\text{ext,max}}$ plotted as function of
 158 the maximum contraction speed with linear fit to nifedipine data. Also shown is the intermediate region (green
 159 bar in **e**). Grey line represents linear fit to the data after equilibration of the cell (blue spheres). All error bars
 160 represent s.e.m.

161

162 Next, we used the quantitative RI transient provided by our laser sensors to assess the effect of the
 163 calcium channel blocker nifedipine (Fig. 4e). While the effect of nifedipine on voltage-gated Ca^{2+} -
 164 channels and subsequent intracellular Ca^{2+} dynamics is well documented^{22,23}, the effect on
 165 contractility (Fig. 4f) is less well understood as it is difficult to access in neonatal and iPS-derived
 166 cardiomyocytes. After administration of nifedipine and following a short period of adaptation,
 167 spontaneously beating neonatal CMs showed strongly reduced contraction and relaxation speeds
 168 (Fig. 4g), consistent with a reduced concentration of cytosolic Ca^{2+} . Furthermore, while we observed

169 that nifedipine increased the pulse-to-pulse variability in Δn_{ext} , the time to reach the maximum
 170 contraction changed only marginally (Fig. 4f). The lower contraction speed was therefore largely
 171 caused by reduced contractility of the cell within the same contraction time which is most likely a
 172 result of the calcium dynamics being only slightly affected by nifedipine²². Interestingly, this leads to
 173 a linear relationship between the mechanical dynamics (contraction speed) and the maximum density
 174 change a cell can produce (Δn_{ext}), with the latter levelling off with increasing maximum contraction
 175 speed (Fig. 4h). Assuming that the saturation contractility of $\Delta n_{\text{ext}} = 0.002$ observed prior to
 176 administration of nifedipine is limited by the number of cross bridges that contribute to force
 177 generation, only about 25% of these cross bridges bind to thin filaments in the presence of 500 nM
 178 nifedipine.



179
 180 **Fig. 5 | Multimodal sensing and *in vivo* integration.** **a**, Extracellular microlaser (white arrow) on top of an adult
 181 CM. Scale bar, 30 μm . **b**, Magnified view showing highly organized myofibrils (sarcomere repeat units indicated
 182 by dashed blue lines). Scale bar, 4 μm . **c**, Averaged profiles of n_{ext}^* (black), SL (blue), and fluorescent calcium
 183 reporter (red). Shaded areas represent s.e.m. of at least 10 contractions. **d-g**, Integration of microlaser into live
 184 zebrafish. **d**, Schematic drawing of microlaser injection. Scale bar, 500 μm . **e**, Microlaser attached to the atrium
 185 of a zebrafish heart (3 dpf). Scale bar, 200 μm . **f**, Magnified view of the microlaser (arrow). V, ventricle; A, atrium.
 186 Scale bar, 50 μm . **g**, n_{ext} (red spheres) and n_{ext}^* (blue line) calculated using sensitivity calibration.

187
 188 Microlaser contractility measurements can also be combined with all-optical electrophysiology
 189 platforms^{22,23}. Simultaneous laser spectroscopy and calcium imaging were performed on fully
 190 differentiated mouse CMs that comprise highly organized myofibrils and a transverse tubular system
 191 ensuring synchronized calcium release and rapid contraction throughout the cell (Figs. 5a and 5b,
 192 Supplementary Video 3). Being non-phagocytic, adult CMs are not able to actively internalise
 193 microlasers; so we instead measured spectral changes in the emission of microlasers that were in
 194 contact with the cell membrane. Transient profiles of single adult CMs again showed contractions as
 195 periodic increases in RI, albeit with smaller amplitude than before (Fig. 5c, Supplementary Fig. 7),
 196 demonstrating that Δn_{ext} depends on the volume overlap of the evanescent component of the lasing

197 mode with the myofibrils. However, consistent with our previous observation, the RI transient showed
198 a direct correlation with sarcomere length (Fig. 5c), confirming a contraction-induced change in
199 myofibril density. We also compared the contractility profile to the profile of cytosolic Ca^{2+} and found
200 a characteristic latency time of 30 ms between calcium signalling and force development while the
201 maximum contraction speed coincided with peak Ca^{2+} concentration (Fig. 5c).

202 Having demonstrated intra- and extracellular sensing *in vitro*, we next implemented our technique in
203 live zebrafish, a model organism with remarkable capabilities to repair and regenerate large fractions
204 of the heart²⁴. Microlasers were injected by a microneedle (Fig. 5d), placing them at the outer wall of
205 the atrium (Figs. 5e and 5f). Extracellular sensing rather than direct intracellular injection was
206 performed to avoid disruption of the myocardium which at this developmental stage consists of a
207 single layer of cardiomyocytes^{25,26} that is not yet covered by the developing epicardium. Lasing
208 wavelengths again showed the typical red-shift associated with cardiomyocyte contraction
209 (Supplementary Fig. 8). Due to increased tissue scattering and rapid movement (Supplementary
210 Video 4), the intensity of individual modes varied strongly, and the lower intensity TM modes were
211 not detected for a large fraction of the contraction cycle. However, after calibrating the sensitivity of
212 the microlaser from time-points that contained a sufficient number of modes (Supplementary Fig. 9;
213 c.f. Fig. 2d), we were able to construct complete contractility profiles for the beating zebrafish heart
214 (Fig. 5g). A measurement performed at a more posterior position of the atrium revealed a significantly
215 longer systolic plateau (Supplementary Fig. 10), demonstrating locally resolved contractility profiles
216 under *in vivo* conditions.

217 Restoring cardiac function after severe heart injury remains a major clinical challenge due to the low
218 capacity of the adult mammalian heart to produce new CMs²⁷. Current regeneration approaches
219 explore the injection of CMs derived from human embryonic stem cells (hESC) or induced pluripotent
220 stem cells (hiPSC) into the injured heart and the growth of cardiac tissue *in vitro*³⁻⁶. Multifunctional
221 probes which monitor the long-term integration of injected cells or engineered tissue are urgently
222 needed. Chemical sensing with dye-based or transgenic calcium and voltage reporters are now
223 routinely used for all-optical electrophysiology^{25,28}. However, despite their importance, these sensors
224 do not provide insights into the mechanical forces developed by the cells. The processes by which
225 engineered and native cardiac tissue couple mechanically therefore remain unknown^{4,29}. Microlaser-
226 based contractility measurements fill this critical gap by monitoring the contractile properties of
227 individual cells during various developmental stages without the need for staining or genetic alteration.
228 Our spectroscopic contractility technique is expected to be more resilient to scattering than imaging-
229 based methods since scattering in biological tissue is elastic and hence does not alter spectral
230 characteristics. Furthermore, the nanosecond-pulsed pumping in combination with single-shot read-

231 out applied here virtually eliminates temporal averaging effects that represent a common source of
232 motion artefacts in intravital confocal or light sheet microscopy.³⁰ This can be combined with recent
233 advances in focussing of light deep into scattering tissue³¹, to achieve remote and non-invasive
234 monitoring of cardiac function *in vivo*. By providing single cell specificity, long-term tracking, and
235 reduced sensitivity to scattering, microlasers introduce new possibilities for translational approaches
236 that extend well beyond current microscopy-based techniques, offer reduced complexity, and impose
237 fewer experimental restrictions.

238 In the future, implementing our recently developed semiconductor WGM nanolasers³² or plasmonic
239 nanolasers^{33,34} will improve and simplify internalization further, eliminate any mechanical restriction
240 of the laser probes and drastically reduce the required pump energy. However, surface passivation,
241 heat management and advanced calibration protocols are needed for these single mode lasers before
242 a comparable degree of bio-compatibility and RI sensitivity can be achieved. Furthermore, using high
243 throughput chip-based devices³⁵ can enable massively parallel integration of lasers into hiPSC- or
244 hESC-derived cardiomyocytes which in turn would facilitate labelling and monitoring of individual cells
245 from the very early stages of the generation of functional cardiac tissue onwards. Likewise, microlasers
246 can offer functional sensing in newly developed stem cell therapies that are able to restore infarcted
247 tissue³⁶.

248 **References**

- 249 1. Aguirre, A. D., Vinegoni, C., Sebas, M. & Weissleder, R. Intravital imaging of cardiac function
250 at the single-cell level. *Proc. Natl. Acad. Sci.* **111**, 11257–11262 (2014).
- 251 2. Kobirumaki-Shimozawa, F. *et al.* Nano-imaging of the beating mouse heart *in vivo*:
252 Importance of sarcomere dynamics, as opposed to sarcomere length per se, in the regulation
253 of cardiac function. *J. Gen. Physiol.* **147**, 53–62 (2016).
- 254 3. Tzahor, E. & Poss, K. D. Cardiac regeneration strategies: Staying young at heart. *Science*
255 (80-). **356**, 1035–1039 (2017).
- 256 4. Shiba, Y. *et al.* Allogeneic transplantation of iPSC cell-derived cardiomyocytes regenerates
257 primate hearts. *Nature* **538**, 388–391 (2016).
- 258 5. Ronaldson-Bouchard, K. *et al.* Advanced maturation of human cardiac tissue grown from
259 pluripotent stem cells. *Nature* **556**, 239–243 (2018).
- 260 6. Liu, Y.-W. *et al.* Human embryonic stem cell-derived cardiomyocytes restore function in
261 infarcted hearts of non-human primates. *Nat. Biotechnol.* **36**, 597–605 (2018).
- 262 7. Ambrosy, A. P. *et al.* The Global Health and Economic Burden of Hospitalizations for Heart
263 Failure: Lessons Learned From Hospitalized Heart Failure Registries. *J. Am. Coll. Cardiol.* **63**,
264 1123–1133 (2014).
- 265 8. Hashimoto, H., Olson, E. N. & Bassel-Duby, R. Therapeutic approaches for cardiac
266 regeneration and repair. *Nat. Rev. Cardiol.* **15**, 585–600 (2018).

- 267 9. Menasché, P. Cell therapy trials for heart regeneration — lessons learned and future
268 directions. *Nat. Rev. Cardiol.* **15**, 659–671 (2018).
- 269 10. Mauranyapin, N. P., Madsen, L. S., Taylor, M. A., Waleed, M. & Bowen, W. P. Evanescent
270 single-molecule biosensing with quantum-limited precision. *Nat. Photonics* **11**, 477–481
271 (2017).
- 272 11. Vollmer, F. & Arnold, S. Whispering-gallery-mode biosensing: label-free detection down to
273 single molecules. *Nat. Methods* **5**, 591–596 (2008).
- 274 12. Kim, E., Baaske, M. D., Schuldes, I., Wilsch, P. S. & Vollmer, F. Label-free optical detection of
275 single enzyme-reactant reactions and associated conformational changes. *Sci. Adv.* **3**,
276 e1603044 (2017).
- 277 13. Schubert, M. *et al.* Lasing within Live Cells Containing Intracellular Optical Microresonators
278 for Barcode-Type Cell Tagging and Tracking. *Nano Lett.* **15**, 5647–5652 (2015).
- 279 14. Humar, M. & Yun, S. H. Intracellular microlasers. *Nat. Photonics* **9**, 572–576 (2015).
- 280 15. Feng, C. *et al.* Organic-Nanowire–SiO₂ Core–Shell Microlasers with Highly Polarized and
281 Narrow Emissions for Biological Imaging. *ACS Appl. Mater. Interfaces* **9**, 7385–7391 (2017).
- 282 16. Wu, X. *et al.* Nanowire lasers as intracellular probes. *Nanoscale* **10**, 9729–9735 (2018).
- 283 17. Liu, P. Y. *et al.* Cell refractive index for cell biology and disease diagnosis: past, present and
284 future. *Lab Chip* **16**, 634–644 (2016).
- 285 18. Irving, T. C., Konhilas, J., Perry, D., Fischetti, R. & de Tombe, P. P. Myofilament lattice spacing
286 as a function of sarcomere length in isolated rat myocardium. *Am. J. Physiol. Circ. Physiol.*
287 **279**, H2568–H2573 (2000).
- 288 19. Yagi, N. *et al.* Sarcomere-length dependence of lattice volume and radial mass transfer of
289 myosin cross-bridges in rat papillary muscle. *Pflugers Arch. Eur. J. Physiol.* **448**, 153–160
290 (2004).
- 291 20. Moeendarbary, E. *et al.* The cytoplasm of living cells behaves as a poroelastic material. *Nat.*
292 *Mater.* **12**, 253–261 (2013).
- 293 21. Schreckenber, R. in *Cardiomyocytes – Active Players in Cardiac Disease* 135–163 (Springer
294 International Publishing, 2016). doi:10.1007/978-3-319-31251-4_5
- 295 22. Klimas, A. *et al.* OptoDyCE as an automated system for high-throughput all-optical dynamic
296 cardiac electrophysiology. *Nat. Commun.* **7**, 11542 (2016).
- 297 23. Dempsey, G. T. *et al.* Cardiotoxicity screening with simultaneous optogenetic pacing, voltage
298 imaging and calcium imaging. *J. Pharmacol. Toxicol. Methods* **81**, 240–250 (2016).
- 299 24. Cao, J. & Poss, K. D. Explant culture of adult zebrafish hearts for epicardial regeneration
300 studies. *Nat. Protoc.* **11**, 872–881 (2016).
- 301 25. Weber, M. *et al.* Cell-accurate optical mapping across the entire developing heart. *Elife* **6**,
302 e28307 (2017).
- 303 26. Brown, D., Samsa, L., Qian, L. & Liu, J. Advances in the Study of Heart Development and
304 Disease Using Zebrafish. *J. Cardiovasc. Dev. Dis.* **3**, 13 (2016).
- 305 27. Vujic, A. *et al.* Exercise induces new cardiomyocyte generation in the adult mammalian heart.
306 *Nat. Commun.* **9**, 1659 (2018).

- 307 28. Jones, J. S., Small, D. M. & Nishimura, N. In Vivo Calcium Imaging of Cardiomyocytes in the
308 Beating Mouse Heart With Multiphoton Microscopy. *Front. Physiol.* **9**, 969 (2018).
- 309 29. Gaetani, R. *et al.* Epicardial application of cardiac progenitor cells in a 3D-printed
310 gelatin/hyaluronic acid patch preserves cardiac function after myocardial infarction.
311 *Biomaterials* **61**, 339–348 (2015).
- 312 30. Vinegoni, C., Lee, S., Aguirre, A. D. & Weissleder, R. New techniques for motion-artifact-free
313 in vivo cardiac microscopy. *Front. Physiol.* **6**, 147 (2015).
- 314 31. Jeong, S. *et al.* Focusing of light energy inside a scattering medium by controlling the time-
315 gated multiple light scattering. *Nat. Photonics* **12**, 277–283 (2018).
- 316 32. Fikouras, A. H. *et al.* Non-obstructive intracellular nanolasers. *Nat. Commun.* **9**, 4817 (2018).
- 317 33. Hill, M. T. & Gather, M. C. Advances in small lasers. *Nat. Photonics* **8**, 908–918 (2014).
- 318 34. Ma, R.-M. & Oulton, R. F. Applications of nanolasers. *Nat. Nanotechnol.* **14**, 12–22 (2019).
- 319 35. Wu, Y.-C. *et al.* Massively parallel delivery of large cargo into mammalian cells with light
320 pulses. *Nat. Methods* **12**, 439–444 (2015).
- 321 36. Lee, A. S. *et al.* Prolonged survival of transplanted stem cells after ischaemic injury via the
322 slow release of pro-survival peptides from a collagen matrix. *Nat. Biomed. Eng.* **2**, 104–113
323 (2018).

324

325 **Acknowledgements** This research was financially supported by the European Research
326 Council under the European Union's Horizon 2020 Framework Programme (FP/2014-
327 2020)/ERC Grant Agreement No. 640012 (ABLASE), by EPSRC (EP/P030017/1) and by the RS
328 Macdonald Charitable Trust. S.J.P. acknowledges funding by the Royal Society of Edinburgh
329 (Biomedical Fellowship) and the British Heart Foundation (Grant FS/17/9/32676). M.S.
330 acknowledges funding by the European Commission (Marie Skłodowska-Curie Individual
331 Fellowship, 659213) and the Royal Society (Dorothy Hodgkin Fellowship, DH160102).

332 **Author contributions** M.S. designed, performed and analysed laser experiments and imaging.
333 L.W. contributed to lasing experiments and B.C. contributed to sarcomere length
334 measurements. I.R.M.B. and L.W. developed refractive index fitting and peak fitting software,
335 respectively. A.M. and M.S. prepared neonatal CM cultures with support from G.B.M. G.B.R.
336 prepared isolated CMs under supervision of S.J.P. S.J.P. and M.S. designed physiological
337 experiments in isolated CMs. C.S.T. supported the preparation of Zebrafish. M.S. and M.C.G.
338 conceived the project and wrote the manuscript with contributions from all authors.

339 **Competing interests** All authors declare no competing interests.

340 **Additional information**

341 **Supplementary information** is available for this paper.

342

343 **Methods**

344 **Animals**

345 The use of experimental animals was approved by the Animal Ethics Committee of the University of St.
346 Andrews and the University of Edinburgh. The care and sacrifice of animals used conformed to Directive
347 2010/63/EU of the European Parliament on the protection of animals used for scientific purposes as well
348 as the United Kingdom Animals (Scientific Procedures) Act 1986.

349 **Cell culture**

350 HL-1 cells were cultured in Claycomb medium (Sigma-Aldrich) supplemented with 100 μ M norepinephrine,
351 10 % (v/v) foetal bovine serum (FBS), 2 mM L-glutamine and 1 % (v/v) penicillin/streptomycin (PS). The cells
352 were stored in T-25 flasks (Fisher Scientific) and incubated at 37°C with 5% CO₂. Prior to seeding, the flasks
353 were coated with gelatine/fibronectin (0.02% gelatine, 1 mg/ml fibronectin) for at least an hour to improve
354 adherence of the cells. Cells were supplied daily with 1 ml of medium per 3.5 cm² of culture area to
355 maintain and maximise the contractile activity.

356 **Isolation and culture of neonatal cardiomyocytes**

357 Neonatal mouse hearts were obtained from postnatal day 2 – 3 C57 laboratory mice. Tissue was collected,
358 cleaned and cut into pieces in ice-cold calcium- and magnesium-free Dulbecco's phosphate buffered saline
359 and digested for 30 min in papain (10 units/ml; Worthington) at 37°C. Treated tissue was dissociated to a
360 single cell suspension by gentle reverse-pipetting in cell culture medium (Dulbecco's Modified Eagle's
361 Medium with 25 mM glucose and 2 mM Glutamax, 10 % (v/v) FBS, 1 % (v/v) non-essential amino acids, 1 %
362 (v/v) PS). Non-disaggregated material was allowed to sediment for 2 minutes and the cell suspension
363 pelleted by centrifugation at 200 x g for 5 min. Pelleted cells were resuspended in cell culture medium and
364 pre-plated on an uncoated cell culture flask for 2 – 4 h to enrich cardiomyocytes through surface-
365 attachment of fibroblasts. The cell culture medium containing unattached cells was then recovered from
366 this flask, cardiomyocytes concentrated by centrifugation and seeded at a density of 2 x 10⁵ cells per dish.
367 Prior to seeding, culture dishes (Ibidi) were coated with 0.02 % gelatin/5 μ g/ml fibronectin. Cultures were
368 kept in a humidified incubator at 37°C, 5% CO₂, 95% air. 1 x 10⁵ microlasers (15 μ m PS-DVB microspheres
369 stained with Firefli Fluorescent Green, uniformity <12%, Thermo Fisher, UK, 11895052) were added to the
370 dish one day after seeding and incubated over night. Lasing experiments were performed within the next
371 1-2 days while cultures showed widespread spontaneous contractions for up to two weeks.

372 **Isolation of adult cardiomyocytes**

373 Adult cardiomyocytes were isolated using an adapted Langendorff-free protocol as previously described.³⁷
374 Isolation solutions used were based on a modified Tyrode's solution: EDTA buffer (in mM): 5 KCl, 130 NaCl,
375 0.5 NaH₂PO₄, 10 HEPES, 10 glucose, 5 Na-pyruvate and 5 ethylenediaminetetraaceticacid (EDTA) titrated
376 to pH 7.8 with NaOH; Perfusion buffer (in mM): 5 KCl, 130 NaCl, 0.5 NaH₂PO₄, 10 HEPES, 10 glucose, 5 Na-
377 pyruvate and 1 MgCl₂ titrated to pH 7.8 with NaOH; Collagenase buffer: 35 mg collagenase type II
378 (Worthington, USA), 50 mg BSA and 15 mg protease (type XIV, Sigma-Aldrich, UK) diluted in 30 ml of
379 perfusion buffer.

380 Adult C57 mice were killed by cervical dislocation, the chest cavity rapidly opened and descending vessels
381 severed. The right ventricle was injected with 7 ml of EDTA buffer over 1 minute to quickly clear residual
382 blood and stop contraction. The ascending aorta was clamped in situ using haemostatic forceps and the
383 heart excised. The heart was then submerged in EDTA buffer, with a further 10 ml injection of EDTA buffer
384 into the left ventricle over 3 minutes. EDTA buffer was cleared by injection of 3 ml of perfusion buffer into
385 the left ventricle. The heart was then submerged in collagenase buffer, and 30-50 ml of collagenase buffer
386 injected into the left ventricle over 10 minutes. Digestion was taken as complete following a marked
387 reduction in resistance to injection pressure. The digested heart was then transferred to a culture dish
388 containing fresh collagenase buffer and trimmed of any excess non-cardiac tissue. Cardiomyocyte
389 dissociation was completed by gentle trituration using a P1000 pipette. Enzymatic digestion was inhibited
390 by addition of perfusion buffer containing 5 % (v/v) FBS (FBS; Thermo Fisher, UK). Isolated cardiomyocytes
391 were reintroduced to Ca²⁺ by three rounds of 20 minutes sequential gravity settling in perfusion buffer
392 containing 300 μ M, 500 μ M, and 1 mM CaCl₂, respectively. Cells were stained (see below) and subsequently
393 transferred into a culture dish (Ibidi) containing 1 mM Ca²⁺ perfusion buffer. After the cells sedimented, 1
394 x 10⁵ microlasers were added to the dish and lasing experiments were performed within 3 hours of isolation.

395

396 **Cardiomyocyte staining**

397 Neonatal cardiomyocytes were labelled with 100 nM SiR-actin overnight. Following isolation, adult
398 cardiomyocytes were loaded with 10 μ M X-Rhod-1 AM (λ_{ex} = 580 nm, λ_{em} = 602 nm; Thermo Fisher, UK) in
399 perfusion buffer containing 1 mM CaCl₂ for 45 minutes at room temperature. Cells were then washed in 1
400 mM Ca²⁺ perfusion buffer and left for 15 minutes at room temperature to allow de-esterification of X-Rhod-
401 1 AM.

402 **Laser spectroscopy**

403 All components for optical pumping and laser spectroscopy were integrated into a standard inverted
404 fluorescence microscope (Nikon, TE2000), equipped with epi fluorescence and differential interference
405 contrast (DIC). The output from a Q-switched and mode-locked diode pumped solid state laser (Alphas) with
406 wavelength, pulse width and repetition rate of 473 nm, 1.5 ns, and 100 Hz, respectively, was coupled
407 into the objective via a dichroic filter and passed to the sample through either a 60x oil immersion or a 40x
408 long working distance objective. In addition, a further 1.5x magnification was used for sarcomere length
409 tracking. The pump laser was focussed to a 15 μ m large spot and a maximum pulse energy of 5-50 nJ was
410 used depending on resonator size and tissue scattering. Emission from the microlaser was collected by the
411 same objective, separated from the pump light by the dichroic and passed to the camera port of the
412 microscope. The image was relayed to a 300 mm spectrometer (Andor) and a cooled sCMOS camera
413 (Hamamatsu) using a series of relay lenses and dichroic beam splitters. The pump laser and spectrometer
414 were synchronized such that each spectrum corresponded to a single pump pulse. During lasing
415 experiments cells were kept in a humidified on-stage incubator system (Bioscience Tools) set to 37°C and
416 purged with 5% CO₂, 95% air.

417 Laser thresholds were acquired on the same setup by varying the pump power with a set of neutral density
418 filters. Below threshold, spectra were integrated over 800 pump pulses while above threshold between
419 100 and 20 pump pulses were used. SNR measurements were performed in a subsequent scan but by
420 integrating over only 1 pump pulse to resemble the conditions of the cardiac measurements. SNR is defined
421 as laser mode peak intensity over fluorescence background.

422 **Confocal microscopy**

423 Confocal imaging was performed on a Leica TCS SP8 laser scanning microscope with 40x and 63x oil
424 immersion objectives. Neonatal CMs were fixed for 10 min in 4% paraformaldehyde, permeabilized with
425 Triton X-100 and subsequently incubated with the primary cardiac troponin T (cTnT) monoclonal antibody
426 (Thermo Fisher, UK, MA5-12960), the secondary Anti-Mouse IgG CF™ 594 antibody (Sigma-Aldrich,
427 SAB4600092), and DAPI. DAPI, microlasers and myofibrils were excited by sequentially scanned continuous
428 wave lasers with a wavelength of 405 nm, 488 nm, and 594 nm, respectively.

429 **Multimodal imaging**

430 In addition to the laser coupling spectroscopy optics, a red bandpass filter placed in the dia illumination
431 path of the microscope, a quad-edge epi-luminescence filter cube and additional band pass filters at the
432 spectrograph and camera allowed simultaneous recording of microlaser lasing spectra, and the epi-
433 fluorescence and DIC imaging of cells. Live cell imaging was performed by using an on-stage incubator
434 system.

435 **Sarcomere length measurements**

436 To determine the average sarcomere length in neonatal mouse cardiomyocytes, myofibrils were
437 fluorescently labelled with SiR-actin (see above) and videos were recorded under epi-illumination
438 conditions at 50 fps using a 60x oil immersion objective (NA 1.4). Raw fluorescence microscopy images
439 were first smoothed by removing statistical noise.³⁸ From the smoothed videos intensity profiles were
440 taken along individual myofibrils, covering 5 to 8 sarcomere units. Profiles were then interpolated by a
441 factor of 10, to facilitate an increase in the spatial resolution of the length measurements to about 10 nm
442 that was otherwise limited by the pixel size of the camera and magnification of the microscope.
443 Interpolated profiles were smoothed using the Savitzky-Golay method. Minima in the intensity profiles
444 were tracked through time at 20 ms intervals. Once the separation between the first and last minima was
445 determined, it was divided by the number of sarcomeres to calculate the average sarcomere length in each
446 frame. In adult cardiomyocytes, sarcomere length measurements were performed using DIC videos
447 recorded at 100 fps by using the ImageJ plugin SarcOptiM.³⁹ Briefly, a fast Fourier transformation algorithm
448 is used to extract the regular spacing in a line profile plotted along the longitudinal axis of the cell. Adult

449 cardiomyocytes were electrically paced at 1 Hz with Platinum wire bath electrodes by applying 8 ms square
450 voltage pulses with a maximum electric field of 30 V/cm.

451 ***In vivo* zebrafish experiments**

452 All zebrafish embryos used in our experiments were under the age of 5 days post fertilisation (dpf).
453 Embryos were collected from random matings and then correctly developmentally staged. Fertilised eggs
454 were transferred at the 2–8 cell stage to 10 cm culture dishes at 28.5°C with systems water replaced every
455 24 h. When necessary, larvae were anaesthetised with MS-222 (tricaine methanesulfonate, 40 µg/ml,
456 Sigma-Aldrich). Microlasers were injected into the sinus venosus region of 3 dpf embryos with a
457 micropipette (pulled on a Sutter P97) attached to a Narishige IM-300 microinjector, whilst viewed on a
458 stage of a Leica M16F stereo microscope. Lasing experiments were performed at room temperature.

459

460 **Data availability**

461 All research data presented in this study will be made available on the University of St Andrews online
462 depository PURE.

463 **Code availability**

464 The custom-made computer code is available from the corresponding authors upon request.

465

466 37. Ackers-Johnson, M. *et al.* A Simplified, Langendorff-Free Method for Concomitant Isolation of
467 Viable Cardiac Myocytes and Nonmyocytes From the Adult Mouse Heart. *Circ. Res.* **119**, 909–
468 20 (2016).

469 38. Carlton, P. M. *et al.* Fast live simultaneous multiwavelength four-dimensional optical
470 microscopy. *Proc. Natl. Acad. Sci.* **107**, 16016–16022 (2010).

471 39. Pasqualin, C. *et al.* SarcOptiM for ImageJ: high-frequency online sarcomere length computing
472 on stimulated cardiomyocytes. *Am. J. Physiol. Physiol.* **311**, C277–C283 (2016).